Efficient electrocatalytic H_2O_2 activation over nitrogen-doped carbon encapsulated Co_3O_4 for drinking water disinfection

Xue Wen [a], Xiangcheng Zhang [a], Meng Wang [b], Congli Yuan [b], Junyu Lang [c,*], Xue Li [a], Hao Wei [a], Daniel Mandler [d], Mingce Long [a,*]

[a] School of Environmental Science and Engineering, School of Electronics, Information and Electrical Engineering, Key Laboratory of Thin Film and Microfabrication Technology (Ministry of Education), Shanghai Jiao Tong University, Shanghai 200240, PR China
[b] School of Agriculture and Biology, Shanghai Jiao Tong University, Shanghai 200240, PR China
[c] School of Physical Science and Technology, ShanghaiTech University, Shanghai 201210, PR China
[d] Institute of Chemistry, the Hebrew University of Jerusalem, Jerusalem 9190401, Israel
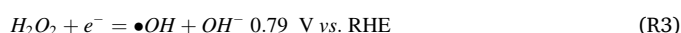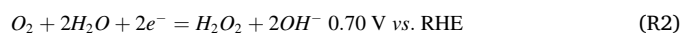
A R T I C L E I N F O

A B S T R A C T

Waterborne diseases claim a million lives each year in areas without adequate centralized water treatment. Electrocatalytic •OH production presents a promising avenue for decentralized water disinfection. However, existing catalysts are limited by low activity at neutral pH and the risk of metal leaching. We have developed a chainmail catalyst, N-doped carbon (NC) encapsulated Co_3O_4 ($NC@Co_3O_4$), for efficient electrocatalytic H_2O_2 activation. Co_3O_4 extracts electrons from NC, thus enhancing the affinity of O atom of H_2O_2 at the electron deficient carbon sites in NC and promoting the cleavage of O−O bonds. Consequently, the •OH generation rate catalyzed by $NC@Co_3O_4$ was 6.5 times of that by NC. Integrating the $NC@Co_3O_4$ into a flow-through electrochemical reactor as cathode, a voltage of only 2 V drove the device to achieve more than 6.8 logs (99.99998 %) of Escherichia coli inactivation in tap water. This work provides an energy-efficient, green, and safe solution for decentralized water disinfection.

1. Introduction

As of 2020, nearly 2 billion people were bereft of secure drinking water[1], especially in remote and scarcely populated areas[2]. As the proliferation of centralized water treatment proves to be an arduous undertaking, infirmities engendered by pathogenic microorganisms carried in water have accounted for the demise of one child every 17 s [3], contributing to a total of over 800,000 fatalities per year [4]. Action is therefore imperative in the advancement of inexpensive decentralized water treatment. UV disinfection [5], electroporation disinfection [6–9] and membrane filtration [10,11] are limited by high cost, energy consumption and equipment maintenance. Solar disinfection is not expensive but time-consuming and weather-constrained [12]. Electro-Fenton technology provides a low energy consumption, green, and safe solution [13–15]. In the electro-Fenton system, air and water can be used as raw materials for H_2O_2 generation with a theoretical voltage of only 0.53 V (**R1** and **R2**) where H_2O_2 can be further activated to form •OH (**R3**). Significant progress has been made in electrocatalytic reduction of O_2 to H_2O_2 [16,17]. However, the disinfection effect of H_2O_2 is relatively

poor. In contrast to H_2O_2, •OH surpasses in disinfectant efficacy by over 7 orders of magnitude [18]. With a towering oxidation-reduction potential of 2.32 V (pH7), •OH can mineralize almost all organic pollutants and eradicate pathogenic microorganisms [18,19]. Activating H_2O_2 to •OH is thus the critical predicament.

$$2H_2O \rightarrow O_2\uparrow + 4H^+ + 4e^- \quad 1.23 \text{ V } vs. \text{ RHE} \tag{R1}$$

$$O_2 + 2H_2O + 2e^- = H_2O_2 + 2OH^- \quad 0.70 \text{ V } vs. \text{ RHE} \tag{R2}$$

$$H_2O_2 + e^- = \bullet OH + OH^- \quad 0.79 \text{ V } vs. \text{ RHE} \tag{R3}$$

A large number of catalysts for H_2O_2 activation are transition metal-based catalysts, for example, Fe_2O_3 [20], Fe_3O_4 [21], FeOCl [22–24], stainless steel [25]. The chemical adsorption between transition metal sites and H_2O_2 lengthens the O−O bond and amplifies its susceptibility to break [26]. Regrettably, these catalysts are only effective in acidic conditions. At neutral pH, the transition metal sites have a strong coordination effect with the OH^- generated by the H_2O_2 decomposition (**R3**), which hinders the turnover of active sites. [25], [27–29].

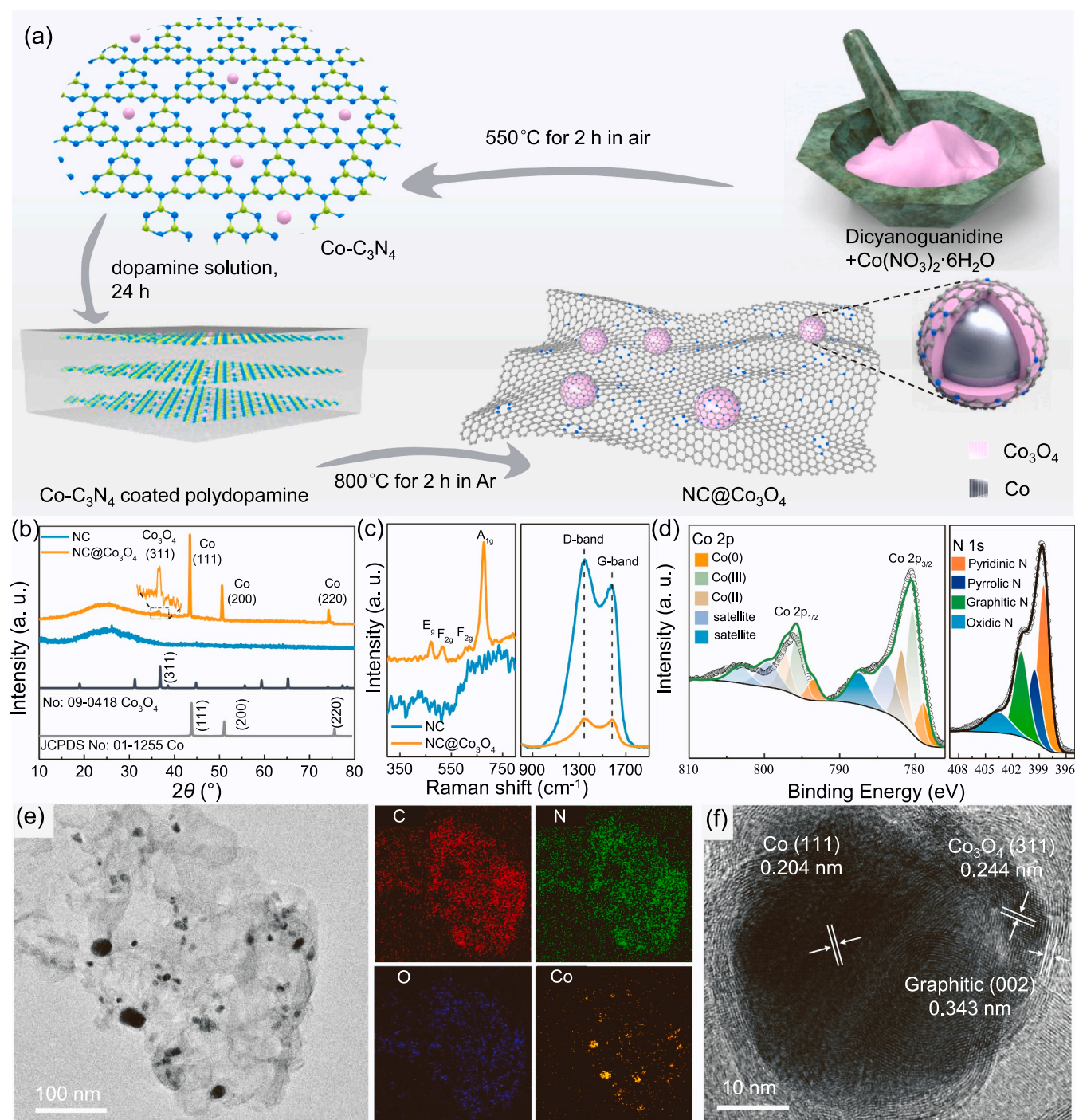**Fig. 1.** Synthesis and structure characterization of NC@Co$_3$O$_4$. (a) Synthesis process and structure illustration of NC@Co$_3$O$_4$. (b, c) XRD and Raman spectra of NC@Co$_3$O$_4$ and NC. (d) XPS of NC@Co$_3$O$_4$. (e) HRTEM of NC@Co$_3$O$_4$ and EDX elemental mapping of C, N, O, Co. (f) HRTEM of the core-shell structure in NC@Co$_3$O$_4$.

Furthermore, the carboxylic acid intermediates, which emerge from the degradation of organic compounds, may also induce the deactivation of metal sites because of their propensity to form complexes with transition metals [30–32]. Limited by the low catalytic activity under neutral pH and leaching of heavy metals, metal-based catalysts are unsuitable for drinking water disinfection. Fortunately, the metal-free catalysts have provided more potential instances of H$_2$O$_2$ activation under neutral pH [33–35]. The carbon atoms adjacent to the heteroatoms usually serve as active centers [36]. This avoids the catalyst poisoning induced by OH$^-$ and carboxylic acids and overcomes the drawbacks of metal-based catalysts. Nevertheless, the weak attraction between the negatively charged

O$^{\delta-}$ of H$_2$O$_2$ and the positively charged C$^{\delta+}$ contributes very little for the cleavage of the O−O bond of H$_2$O$_2$. It is necessary to further improve catalytic activity of metal-free catalysts.

Chainmail catalysts, which vividly describe a metal-based catalyst encapsulated in a non-metallic shell, can amalgamate the merits of both metallic and non-metallic catalysts [37,38]. The non-metallic shell shields the internal metallic structure from poisoning as well as leaching, whilst the internal metallic structure regulates the electronic structure of carbon shells via unique electron penetration effects and charge transfer of heterojunction [39,40]. To fabricate high-performance chainmail catalysts for electrocatalytic H$_2$O$_2$

activation, we selected pyridinic nitrogen-doped carbon (NC) as the chainmail considering its proven effectiveness in H_2O_2 activation [41–43], and encapsulated Co_3O_4 within NC to fabricate a p-n heterojunction, thus intensifying the interaction between the NC and H_2O_2 by minimizing electron density of n-type NC. This chainmail catalyst displayed enhanced activity for electrocatalytic H_2O_2 activation and •OH production, thus achieving efficient water disinfection. Hence, this electrochemical disinfection system based on efficient electrocatalytic •OH generation at neutral pH is promising to solve the drinking water security in population dispersed areas.

2. Experimental section

2.1. Catalyst synthesis

Firstly, cobalt and oxygen co-doped graphitic carbon nitride (Co-C_3N_4) were obtained by thermal polymerization of dicyandiamide and $Co(NO_3)_2 \cdot 6\,H_2O$. Next, the surface was coated with polydopamine through the alkaline-catalyzed polymerization of dopamine. Finally, NC@Co_3O_4 chainmail catalysts were obtained through pyrolysis (Fig. 1a). Specifically, 0, 0.1, 0.5, 1, 2, 10 mmol of $Co(NO_3)_2 \cdot 6\,H_2O$ were dissolved in an appropriate volume of aqueous ethanol. The resulting solution was then mixed well with 10 g of dicyandiamide in an agate mortar. The mixture was subsequently dried, with water and ethanol evaporated at 60 °C while grinding every two minutes, to produce a precursor. The precursor was loaded into a covered ceramic crucible and subjected to air reaction at 550 °C for 2 h, with a heating rate of 5 °C/min, to obtain Co-C_3N_4. Next, 2 g of Co-C_3N_4 and 0.4 g of dopamine hydrochloride (PDA) were dispersed in 80 ml of deionized water, and 6 ml of $NH_3 \cdot H_2O$ were added to initiate dopamine polymerization. The mixture was continuously stirred at 40 °C for 24 h to produce dopamine-coated Co-C_3N_4, named Co-C_3N_4 @PDA. Following this, heat treatment of the obtained sample was performed in an argon atmosphere at 700 °C, 800 °C, and 900 °C for 2 h, with a heating rate of 10 °C/min. The final sample was designated as NC@Co_3O_4-x-y, where x represents the dosages of $Co(NO_3)_2 \cdot 6\,H_2O$ used, and y represents the heat treatment temperature. In order to facilitate the discussion, NC@Co_3O_4-1–800 was further abbreviated as NC@Co_3O_4. NC@Co_3O_4-H500 and NC@Co_3O_4-H800 were obtained by subjecting NC@Co_3O_4 to heat treatment in a 5 % hydrogen-argon atmosphere. The reaction conditions were set to 500 °C for 30 min and 800 °C for 1 h, respectively. The heating rate was 5 °C/min, and the gas flow rate was maintained at 80 ml/min. The synthesis of the catalyst with surface cobalt sites, referred to as "surface Co", was as follows: 35.6 mg of cobalt acetylacetonate was dissolved in 10 ml of water, and then 100 mg of C_3N_4 @PDA was added to the solution. The mixture was stirred for 2 h. Subsequently, the solution was subjected to freeze-drying to obtain the precursor. The precursor was then treated at 800 °C under the same reaction conditions as the preparation of NC@Co_3O_4. FeOCl was prepared by heating $FeCl_3 \cdot 6\,H_2O$ at 220 °C for 2 h with a heating rate of 10 °C/min (Fig. S1)[44].

2.2. Electrode preparation

To prepare the electrodes, the catalyst powder was formulated into an ink using the following components: 5 mg of the catalyst, 700 μl of isopropanol, 280 μl of water, and 20 μl of a 5 wt% Nafion solution. For RRDE (Rotating Ring-Disk Electrode) testing, 6 μl of the ink is spin-coated onto the surface of the RRDE and allow it to air dry naturally. For •OH quantification in the single-cell reactor, 50 μl of the ink is drop-cast onto a 1 cm² hydrophobic carbon paper surface. For the micro flow-through reactor testing, drop-cast 200 μl of the ink onto a graphite felt with a diameter of 1 cm and a thickness of 2 mm. Then, dry the electrode using an infrared lamp. The synthetic method of the IrO_2-Ti electrode was adapted from an electroplating procedure with slight modifications [19]. 150 mg of $IrCl_4 \cdot H_2O$ and 0.5 g of oxalic acid were added into a

stirring solution containing 1 ml of 30% H_2O_2. Then, potassium carbonate was added to adjust the pH to 10.5. The mixture was heated at 90 °C for 15 min and then cooled to room temperature. A three-electrode system was used for electrodepositing IrO_2, with both the working and counter electrodes being titanium mesh. Cyclic voltammetry (CV) scans were performed within the potential range of − 1–1 V vs. Ag/AgCl for 1 h.

2.3. Analytical methods

X-ray diffraction (XRD-6100, Shimadzu) and transmission electron microscopy (TALOS F200X, Thermo Fisher) were utilized to characterize the crystal structure, morphology, and elemental distribution of the catalyst. The surface chemical state of the elements was determined by X-ray photoelectron spectroscopy (Axis Ultra DLD, Shimadzu), where the binding energy of 284.4 eV was defined as the total peak energy for C=C and C−C, and the binding energy of all elements was calibrated accordingly. The Raman spectra were collected with a Bruker Sentera R200-L dispersive Raman microscope at a wavelength of λ = 532 nm. The specific surface area of the samples was measured by the nitrogen adsorption instrument (ASAP2020) using the Brunauer-Emmett-Teller (BET) method. The degassing temperature was set at 180 °C for 5 h. NH_3-TPD was conducted on a temperature-programmed desorption analyzer (Micromeritics AutoChem II 2920). Specifically, the gas was saturated with ammonia at 50 °C, and then NH_3 desorption was executed in a helium atmosphere with a heating rate of 10 °C/min up to 500 °C. The zeta potential of the samples was measured by the Zeta potential-nano particle size analyzer (Delsa Nano C, beckman coulter). Electron paramagnetic resonance (EPR) signals of •OH generated were identified by a Bruker micro EPR spectrometer with DMPO as spin trapping agents. Inductively coupled plasma atomic emission spectroscopy (iCAP6300, Thermo Fisher) was employed to measure the leaching of Co during the reaction process. The quantitative measurement of •OH was performed using 10 mM benzoic acid (BA) as a probe, and the concentration of para-hydroxybenzoic acid (*p*-HBA) was determined by high-performance liquid chromatography (HPLC) equipped with a Shim Pack C18 chromatographic column and a UV detector. A mobile phase consisting of a binary mixture of methanol and 0.1 wt% aqueous phosphoric acid solution with a volume ratio of 4:6 was used. The oven temperature was maintained at 35 °C, and the flow rate was set at 0.9 ml/min. Detection was carried out at 255 nm. The hydroxyl radical concentration was calculated using the following formula (Eq. 1)[45]:

$$C_{\bullet OH} = C_{p-HBA} \times 5.87 \qquad (1)$$

2.4. Drinking water disinfection experiment

A solution of Escherichia coli (BL21, weidibio) with a concentration of approximately 1.0×10^{10} colony-forming units per milliliter (c.f.u./ml) was dispersed in sterilized tap water to simulate bacterial contamination, without the addition of any extra electrolytes. Prior to inactivation, the E. coli concentration in the suspension was measured to be 1.29×10^7 c.f.u./ml. After 5 mM H_2O_2 was added. The model water was passed through a microreactor at a flow rate of 1 ml/min using an injection pump, and the voltage was set to 2 V. To record current changes, the voltage was provided by the electrochemical workstation (Shanghai Chenhua CHI760E). The electrodes were specially linked to the workstation ports (Fig. S2). After 10 min of continuous operation, 1 ml of treated water was collected, serially diluted three times with each dilution differing by 10-fold, and plated on nutrient agar plates. Before and after the reaction, the E. coli concentration was determined using the plate count method. Three independent trials were conducted, and the mean value was calculated.
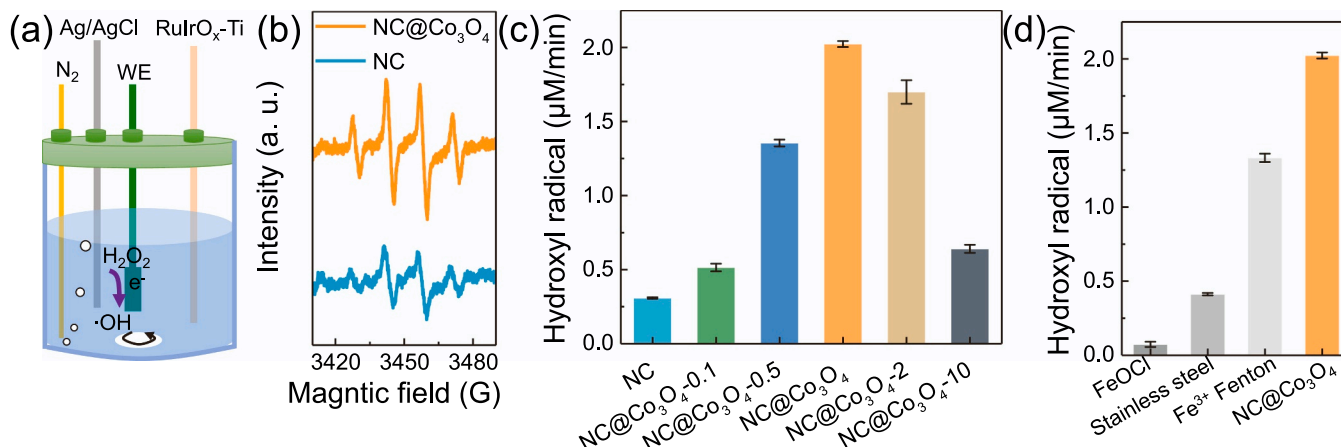
Fig. 2. Performance of electrocatalytic H$_2$O$_2$ activation. (a) The single-cell reactor for quantifying •OH. Working electrode (WE): 0.25 mg catalyst loaded with 1×1 cm^2 carbon paper. Potential: -0.6 V. Solution: 0.1 M NaClO$_4$, 5 mM H$_2$O$_2$, 10 mM benzoic acid (BA) saturated with N$_2$, pH 7.0, 40 ml. Counter electrode: 2×2 cm^2 RuO$_x$ and IrO$_x$ modified Titanium sheet (RuIrO$_x$-Ti) was used to avoid one-electron water oxidation (b) Electron paramagnetic resonance spectroscopy of generated •OH. 5 mM H$_2$O$_2$, 25 mM DMPO, -0.6 V. (c) The rate of •OH generation catalyzed by catalysts with different Co contents. (d) Performance comparison with star catalysts. Fe^{3+} Fenton-like: 100 µM Fe^{3+}, initial pH 2.66.

2.5. Theoretical calculation

The Vienna Ab initio Simulation Package (VASP) was used to perform theoretical calculations[46]. The electron exchange and correlation energy was treated using the generalized gradient approximation in the Perdew-Burke-Ernzerhof functional (GGA-PBE) [47]. Monkhorst Pack k-point grid was set to $2 \times 2 \times 1$. Vaspkit was used to model the NC-Co$_3$O$_4$ heterojunction [48]. The model's lattice parameters were set as follows: a=b= 11.379 Å, c= 27.609 Å, $\alpha = \beta = 90°$, $\gamma = 60°$, and the lattice mismatch was calculated to be 0.927 % (Fig. S3). The spin polarization was considered by setting the ISPIN parameter to 2. The energy cutoff was set to 400 eV. In the geometry optimization process, the atomic positions were fully relaxed until the energy and force converged to within 1×10^{-5} eV and 0.03 eV/Å, respectively. The Climbing Image-NEB (CI-NEB) method was used to initialize the transition state[49], and Dimer method was used to optimize the transition state structure [50]. The reaction Gibbs free energy was calculated by the Eq. 2. The standard hydrogen electrode approximation is used to calculate the Gibbs free energy of proton-electron pair (Eq. 3).

$$\Delta G = \Delta E + \Delta E_{ZPE} - T\Delta S - eU + 0.0592pH \qquad (2)$$

$$G(H^+) + G(e^-) = 0.5 \times G(H_2) - eU + 0.0592pH \qquad (3)$$

where ΔE is the electron energy difference obtained from the DFT calculation, ΔE_{ZPE} and ΔS are the change values of the zero-point energy and entropy, respectively, obtained from the vibration frequency calculation, and the entropy correction value of the gas molecule can be obtained from the standard database. T is the system temperature of the reaction (298.15 K). The "e" represents a single elementary charge, which has a value of -1. U is the applied electrode potential vs. SHE, which is -0.402 V (-0.6 V vs. Ag/AgCl). The reaction pH of this work is 7.

3. Results and discussion

### 3.1. Structural characterization of catalysts

The main component of the catalyst is nitrogen doped carbon. The wide peak in the range of 20–30 degrees in the XRD spectrum correspond to low crystallinity carbon (Fig. 1b), and the Raman spectroscopy shows typical characteristics of carbon materials (Fig. 1c), with a peak at 1350 cm^{-1} for defect carbon and 1580 cm^{-1} for sp^2 carbon. The

increase in cobalt content reduced the content of defect carbon, as reflected in the I_D/I_G decreased from 1.14 to 1 (Fig. S4). The N element is uniformly distributed on the surface (Fig. 1e), and XPS shows that the N mainly exists in the form of pyridinic N, with a content of 6.5 at% (Fig. 1d). The sharp characteristic peaks of metallic cobalt (Co(0)) in the XRD spectrum suggest that most of the cobalt in the catalyst is reduced to form cobalt nanoparticles, leading to the presence of magnetism in the sample (Fig. S5). However, XPS analysis shows that cobalt mainly exists as Co(II) and Co(III), while only a weak signal of Co(0) is detected [51]. The characteristic peaks at 471, 515, 614, and 678 cm^{-1} in the Raman spectrum correspond to the E$_g$, F$_{2g}$, F$_{2g}$ and A$_{1g}$ vibrations of Co$_3$O$_4$, respectively (Fig. 1c) [52,53]. This indicates that the surface of cobalt nanoparticles is enveloped by Co$_3$O$_4$. HRTEM further confirms the Co-Co$_3$O$_4$-carbon core-shell structure (Fig. 1f). The internal lattice stripe spacing of the nanoparticles is 0.204 nm, corresponding to the cobalt (111) crystal plane. A lattice stripe with a crystal plane spacing of 0.244 nm was observed on the surface of the cobalt core, which well matches the (311) crystal plane of Co$_3$O$_4$ and is consistent with the XRD results. The surface of cobalt tetroxide is further coated with carbon layers, with a crystal plane spacing of 0.343 nm. In summary, the chainmail catalyst NC@Co$_3$O$_4$ with NC-Co$_3$O$_4$ heterojunction was successfully prepared.

3.2. Efficient electrocatalytic H$_2$O$_2$ activation for water disinfection

We synthesized a series of samples by adjusting calcination temperature and cobalt dosages to optimize synthetic conditions. Theelectrocatalytic performance was quickly evaluated by the rotating ring disk electrode method [54]. At the same synthesis temperature, as the cobalt dosage increases, the reduction rate of H$_2$O$_2$ and the rate of •OH generation first increase and then decrease (Fig. S6a-c). For the same sample, a more negative potential results in faster H$_2$O$_2$ reduction and •OH generation. To avoid the potential hydrogen evolution reaction (HER), we compared the performance of different catalysts at -0.6 V (0.01 V vs. RHE). The NC@Co$_3$O$_4$ exhibited the best performance (Fig. S6d).

The performance of the catalysts in electrocatalytic activation of H$_2$O$_2$ to produce •OH radicals was evaluated in a single cell reactor, which maintained a constant pH of the solution (Fig. 2a). Nitrogen saturation eliminated possible interference from oxygen reduction reactions in the experiment. The large size of the counter electrode reduced the anode potential, thereby avoiding the anodic oxidation of the probe molecules. DMPO was added to the solution as a •OH capture agent, and the EPR signal of DMPO−OH was detected, proving the
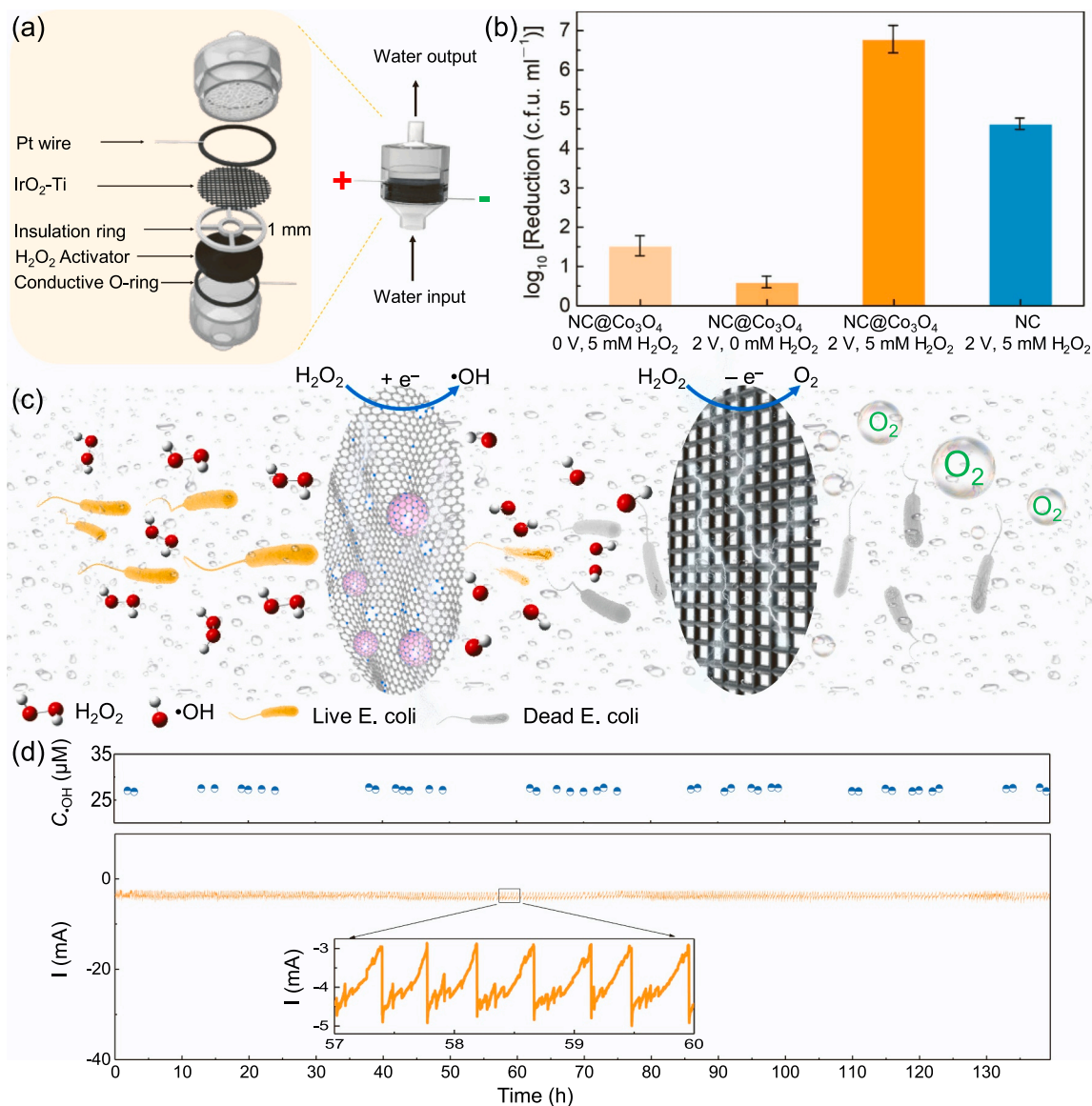
Fig. 3. (a) Flow-through reactor for tap water disinfection. (b) Disinfection performance of tap water. The initial concentration of Escherichia coli is 1.29×10^7 c.f.u. ml^{-1}. (c) Schematic drawing of Escherichia coli inactivation. (d) Stability testing of micro disinfection system. Catalyst: $NC@Co_3O_4$, voltage: 2 V, solution: tap water, containing 5 mM H_2O_2, 10 mM benzoic acid (BA), pH 7.0.

generation of •OH. A higher signal intensity of $NC@Co_3O_4$ implies the more •OH generation (Fig. 2b). Benzoic acid was used as a probe molecule to quantify the rate of •OH generation. The rate of •OH generation was observed to follow a volcano-shaped trend upon increasing the amount of cobalt used in the synthesis of the catalysts (Fig. 2c). This observation can be attributed to the fact that although cobalt can improve the catalytic activity of each active site, an increasing amount of cobalt added to the catalyst composition leads to a decrease in the specific surface area of the catalyst (Fig. S7). Consequently, the number of active sites available for catalysis also decreases, ultimately leading to a reduction in the overall efficiency of the catalytic process. We compared the performance of $NC@Co_3O_4$ with the reported catalysts FeOCl[44]‚[22]‚[24], stainless steel [25,55], and iron ions (Fig. 2d). The •OH generation rate of $NC@Co_3O_4$ reach up to 2 μM/min, about 4 times that of a stainless-steel cathode and 14 times that of a well-known heterogeneous electro-Fenton material FeOCl. It is even 1.5 times higher than that of traditional homogeneous Fenton.

$NC@Co_3O_4$ was applied for water disinfection. The experiment was conducted in a self-made flow-through reactor (Fig. 3a). The catalyst

was loaded on a 2 mm thick graphite felt surface and then used as the cathode. The anode was a titanium mesh coated with IrO_2, and the distance between the two electrodes was controlled by an insulation ring to 1 mm, reducing the solution resistance as much as possible while preventing short circuits. Escherichia coli was dispersed in heat sterilized tap water with an initial concentration of 1.29×10^7 c.f.u. ml^{-1}. 5 mM H_2O_2 was added to the tap water without any additional electrolytes. The reactor was driven by a constant DC voltage of 2 V. After flowing tap water through the reactor at a flow rate of 1 ml/min from bottom to top, the optimal bacterial removal rate was as high as 99.99998% (Fig. 3b). By comparing the conditions of no electricity (column 1) and no H_2O_2 (column 2), it was found that the •OH generated by electrochemical activation of H_2O_2 at the cathode was the reason for sterilization. The sterilization amount of the catalyst $NC@Co_3O_4$ is more than 6.8 log removal of Escherichia coli, which is two orders of magnitude higher than NC (4.6 log). This indicates that an increase in •OH concentration leads to a leap in disinfection performance. Fig. 3c shows the schematic drawing of the Escherichia coli inactivation. The residual H_2O_2 was ultimately anodized and decomposed into O_2. In
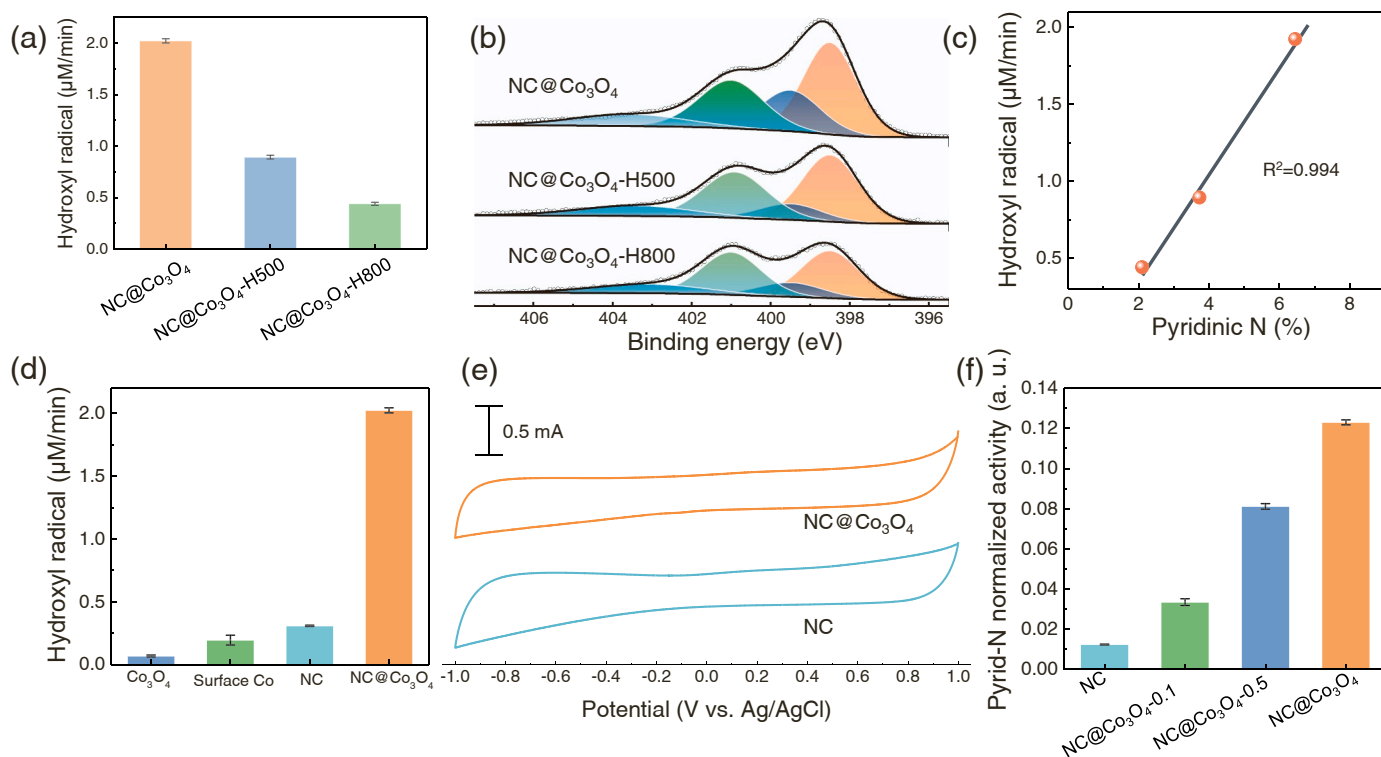
Fig. 4. Determination of catalytic active sites. (a) Comparison of performance before and after hydrogen treatment. NC@Co$_3$O$_4$-H500 and NC@Co$_3$O$_4$-H800, heat treatment at 500 °C and 800 °C in hydrogen gas, respectively. (b) Changes in nitrogen species measured by XPS after hydrogen treatment. (c) The correlation between pyridinic nitrogen content and •OH production. (d) Comparison of performance with catalysts containing cobalt on the surface. (e) CV curve in 0.1 M NaClO$_4$ and N$_2$ saturated solution. (f) The effect of cobalt doping on the activity of pyridinic N sites. The activity is normalized by the pyridinic N content and electrochemical surface area.

addition, the utilization of the reactor for removing soluble organic compounds in lake water shows promising results. The three-dimensional fluorescence spectra further confirm the effectiveness of our system in removing organic substances from the lake water (Fig. S8). This indicates the potential application of the reactor for water purification.

The stability of the micro flow-through system was evaluated by adding benzoic acid as an •OH probe to tap water. During a continuous 140 h test, the current was maintained at a periodic range of 3–5 mA (Fig. 3d). The periodic change of current is because the peristaltic pump acts as the driving force of tap water flow. Sampling and testing the concentrations of •OH at a certain interval of time, show that the concentration of •OH remains approximately 27 μM. The stable current and •OH concentration indicate the high stability of the catalyst and disinfection system. The Co concentration in the effluent was determined by ICP to be 1.4 μg/l, which is much lower than the regulation of 50 μg/l in the Chinese Drinking Water Standard (GB 5749–2022), indicating the safety of the electrochemical water disinfection system. Furthermore, after immersing NC@Co$_3$O$_4$ in aqua regia and subjecting it to a high-pressure reaction at 90 °C for 12 h, the catalyst retained its strong magnetism (Fig. S9). This can be attributed to the effective protection provided by the outer NC shell to the internal Co$_3$O$_4$/Co core. The results highlight the exceptional acid resistance and corrosion resistance exhibited by the chainmail catalyst.

3.3. Mechanism of electrocatalytic H$_2$O$_2$ activation

To determine the catalytic active site, NC@Co$_3$O$_4$ was used as the control sample to heat treatment in hydrogen. After hydrogen treatment, the generation of •OH significantly decreased (Fig. 4a). XPS confirmed that the content of the pyridinic N significantly decreased after hydrogen treatment (Fig. 4b). The linear correlation between the

content of the pyridinic N and •OH generation rate was found by fitting, suggesting that the pyridinic N is the active site. Since metals are usually used as the active sites in catalytic reactions, the possibility of Co as surface active site is also considered. Co$_3$O$_4$ has very low catalytic activity, which indicates that Co$_3$O$_4$ in NC@Co$_3$O$_4$ cannot directly activate H$_2$O$_2$. Cobalt acetylacetone was dispersed on the surface of polydopamine coated C$_3$N$_4$, and then the catalyst with surface Co site was obtained by thermal polymerization. Its performance is lower than NC, indicating that Co is not an active site. The CV curve can sensitively detect surface Co sites [56]. However, the CV curves of NC@Co$_3$O$_4$ and NC are similar, and no redox peak of Co was found, further indicating that the Co species are encapsulated by carbon layers and do not exist on the catalyst surface (Fig. 4e). This explains the stability of the catalyst and the extremely low cobalt dissolution. To illustrate the effect of cobalt on catalytic activity, we compared the activity of catalysts with different cobalt contents through normalization of pyridine nitrogen content and electrochemical active area (Fig. 4f, Fig. S10, equation S1). As the cobalt content increases, the normalization activity also increases. HRTEM demonstrated that an increase in cobalt content increased the proportion of core-shell structure without causing any other structural changes (Fig. S11). The above results indicate that Co does not directly play a catalytic role, but the introduction of cobalt enhances the catalytic activity of the pyridinic N sites.

To understand the influence of Co on the catalytic activity of pyridinic N, we examined the impact of Co addition on the electronic structure of pyridinic N. With increasing Co content, the XPS peaks corresponding to N shift towards higher binding energy (Fig. 5a). Simultaneously, the peak corresponding to C−N bonds in the C 1s spectrum is also observed to shift towards higher binding energy (Fig. 5b). These shifts indicate that the introduction of Co results in the reduction of electrons around N, making it more difficult for N to lose electrons. In the infrared spectrum, the introduction of Co causes the
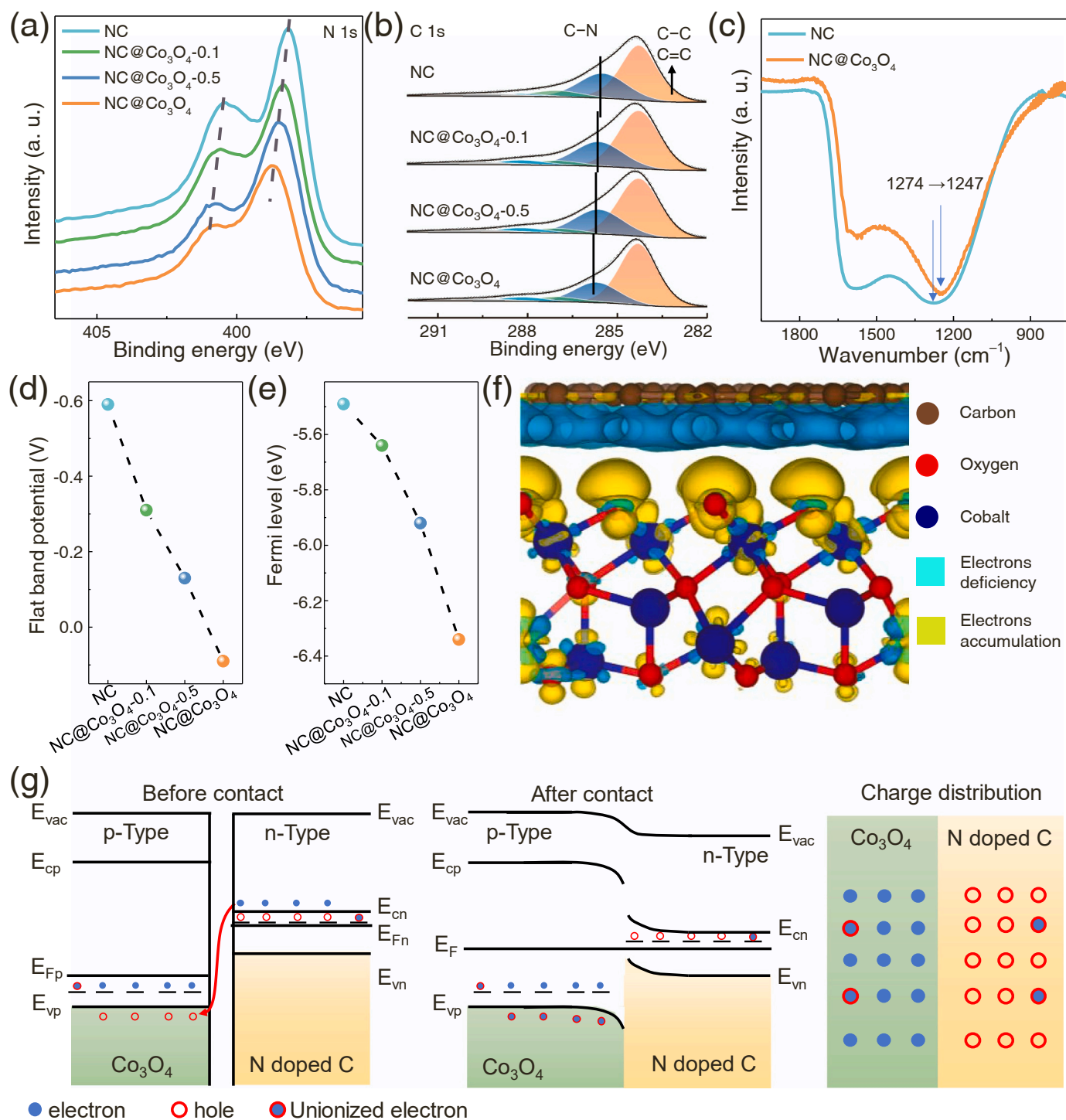
Fig. 5. The effect of Co_3O_4 on the electronic structure of NC. (a, b) XPS of N 1 s and C 1 s, respectively. (c) Infrared spectroscopy. (d) The flat band potential measured by the Mott-Schottky curve. (e) Fermi level measured by UPS. (f) Differential charge density of Co_3O_4 and NC p-n heterojunction. (g) Schematic drawing of energy band and electron transfer of Co_3O_4 and NC p-n heterojunction.

vibrational peak associated with C−N bonds to redshift from 1274 to 1247 cm^{-1}, suggesting weakened C−N bonds (Fig. 5c). This weakening is attributed to the loss of bonding electrons from the C−N bond. The Mott-Schottky curve exhibits a positive slope, indicating the n-type semiconductor behavior of N-doped carbon (Fig. S12). The potential of the semiconductor measured against a reference electrode in the solution is referred to as the flat band potential (E_{fb})[57]. Consequently, the flat band potential positively correlates with the Fermi level. An increase in Co content leads to a more positive flat band potential, signifying a

decrease in the Fermi energy level (Fig. 5d). We also measured changes in the work function of the catalysts using UPS and calculated the Fermi level (Fig. S13). The obtained results further validate that an increased Co content results in a decreased Fermi level (Fig. 5e). All four aforementioned characteristics collectively confirm that Co_3O_4 leads to a reduction in the charge density of pyridinic N.

The differential charge density demonstrates that, at the interface of the NC and Co_3O_4 heterojunction, the electrons of the NC are transferred to the Co_3O_4 (Fig. 5f). Furthermore, the bader charge calculation shows
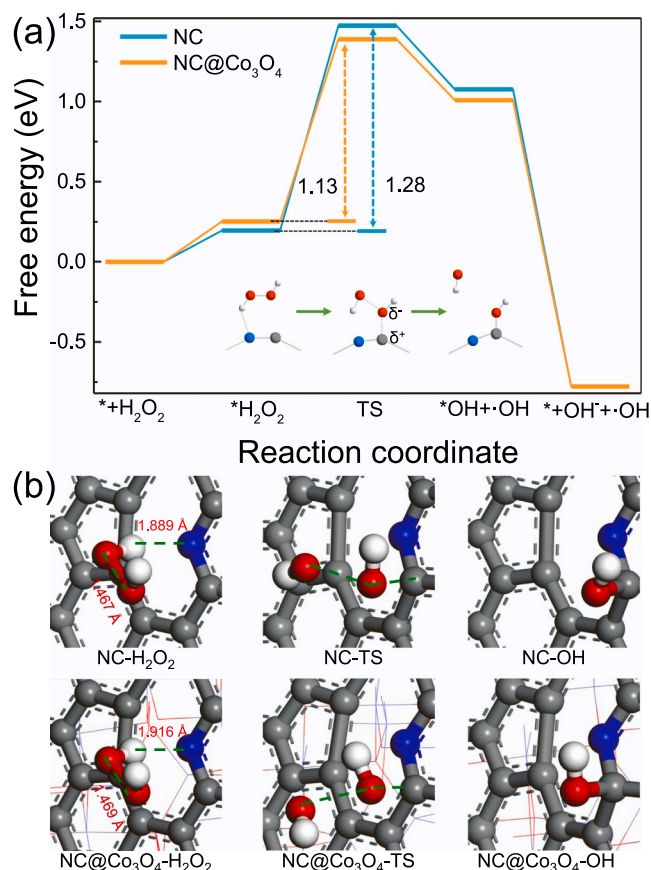
Fig. 6. The theoretical calculation of electrocatalytic H_2O_2 activation. (a) Free energy diagram for electrocatalytic H_2O_2 activation to •OH. (b) The models of adsorbed H_2O_2, transition states (TS), adsorbed OH.

that compared to NC, the carbon atoms adjacent to pyridinic nitrogen of NC@Co$_3$O$_4$ carry more positive charges (Fig. S14). The semiconductor energy band theory explains the electron transfer phenomenon well (Fig. 5g). When the two phases (NC and Co$_3$O$_4$) come into contact, free electrons would transfer from the n-type NC to the p-type Co$_3$O$_4$. As a result, negative charges remain in Co$_3$O$_4$ while positive charges remain in NC. According to the zeta potential test, the zero-charge point of NC@Co$_3$O$_4$ (5.85) is lower compared to NC (6.20), indicating a stronger OH$^-$ adsorption (Fig. S15). The NH$_3$-TPD test results show that NH$_3$ desorption occurs at a higher temperature on the surface of NC@Co$_3$O$_4$ (430 °C) compared to NC (360 °C), suggesting a stronger NH$_3$ adsorption (Fig. S16). Since O and N in the N-doped carbon carry negative charges, the adsorption sites for NH$_3$ and OH$^-$ can only be positively charged carbon atoms. Therefore, it is plausible that the introduction of Co$_3$O$_4$ results in an increased positive charge on the C atoms, leading to enhanced adsorption of OH$^-$ and NH$_3$.

DFT calculations were employed to investigate the mechanism underlying the enhancement of H_2O_2 activation. Initially, H_2O_2 adsorbs onto the catalyst surface, forming a hydrogen bond between its H atom and pyridinic N atom (R4). Subsequently, the positively charged carbon tends to bond with the negatively charged oxygen, causing that C and O are close to each other while the two O are far away from each other (Fig. 6a). This configuration facilitates the catalytic decomposition of the adsorbed H_2O_2, generating •OH and *OH intermediate species (R5). Finally, *OH is reduced to OH$^-$, concluding the complete electrocatalytic process (R6). The O−O bond length of the H_2O_2 adsorbed on NC@Co$_3$O$_4$ is longer than the O−O bond length on NC. This elongation suggests that the O−O bond in the H_2O_2 molecule adsorbed on NC@Co$_3$O$_4$ is weaker, making it more susceptible to breakage (Fig. 6b). Moreover, the activation energy for the decomposition of H_2O_2

decreased from 1.28 eV to 1.13 eV (Fig. 6a). These results provide an explanation for the increased catalytic activity observed in NC@Co$_3$O$_4$. The enlongaed O−O bond and decreased activation energy indicate that H_2O_2 is more easily activated by the NC@Co$_3$O$_4$ catalyst, leading to improved catalytic performance.

$$* + H_2O_2 = *H_2O_2 \qquad (R4)$$

$$*H_2O_2 = *OH + \bullet OH \qquad (R5)$$

$$*OH + e^- = * + OH^- \qquad (R6)$$

4. Conclusion

This article proposes an electrochemical scheme for decentralized water disinfection. The implementation of this scheme is based on two key points, the electrocatalyst and the reactor. The catalyst NC@Co$_3$O$_4$, with a pyridinic N content of 6.5 at% and a surface area of 200 m^2/g, has abundant catalytic sites (the C atom adjacent to pyridinic N). Co$_3$O$_4$ are encapsulated inside the NC layers, ensuring the stability and biosafety of the catalyst. Co$_3$O$_4$ and NC form a p-n junction, which increases the positive charge density of the C, thereby greatly increasing the intrinsic activity of the active center. The efficient activation of H_2O_2 by NC@Co$_3$O$_4$ at neutral pH makes electrochemical water disinfection possible. The flow-through reactor overcomes the short diffusion distance of •OH, allowing sufficient contact of •OH and E. coli and effectively killing them. With an electrode distance of 1 mm, the solution resistance was greatly reduced. Finally, 99.99998 % E. coli inactivation efficiency was achieved by applying a 2 V voltage. As numerous excellent results have been achieved in the production of H_2O_2 by electroreduction of oxygen, by connecting an H_2O_2 electrosynthesis device in series at the front of our efficient •OH generation device, water disinfection can be achieved solely relying on air and electricity.

CRediT authorship contribution statement

Xue Wen: Data curation, Methodology, Investigation, Visualization, Writing-original draft. **Xiangcheng Zhang**: Methodology, Investigation, Visualization. **Meng Wang**: Resources, Investigation, Validation. **Congli Yuan**: Methodology, Investigation, Validation. **Junyu Lang**: Resources, Methodology, Software, Investigation, Validation, Writing - review & editing. **Xue Li**: Investigation, Methodology, Validation. **Hao Wei**: Resources, Validation. **Daniel Mandler**: Resources, Validation, Writing - review& editing. **Mingce Long**: Conceptualization, Supervision, Funding acquisition, Resources, Writing - review & editing.

Declaration of Competing Interest

The authors declare that they have no known competing financial interests or personal relationships that could have appeared to influence the work reported in this paper.

Data availability

Data will be made available on request.

Acknowledgments

Appendix A. Supporting information

Supplementary data associated with this article can be found in the online version at doi:10.1016/j.apcatb.2023.123437.

References

[1] M. Naddaf, The world faces a water crisis – 4 powerful charts show how, Nature 615 (2023) 774–775.

[2] B.C. Hodges, E.L. Cates, J.H. Kim, Challenges and prospects of advanced oxidation water treatment processes using catalytic nanomaterials, Nat. Nanotechnol. 13 (2018) 642–650.

[3] J. Rockström, M. Mazzucato, L.S. Andersen, S.F. Fahrländer, D. Gerten, Why we need a new economics of water as a common good, Nature 615 (2023) 794–797.

[4] The water crisis is worsening. Researchers must tackle it together, Nature, 613 2023. pp. 611–612.

[5] M.A. Shannon, P.W. Bohn, M. Elimelech, J.G. Georgiadis, B.J. Marinas, A. M. Mayes, Science and technology for water purification in the coming decades, Nature 452 (2008) 301–310.

[6] Z.Y. Huo, Y.J. Kim, I.Y. Suh, D.M. Lee, J.H. Lee, Y. Du, S. Wang, H.J. Yoon, S. W. Kim, Triboelectrification induced self-powered microbial disinfection using nanowire-enhanced localized electric field, Nat. Commun. 12 (2021) 3693.

[7] A. Feng, J. Feng, W. Xing, K. Jiang, W. Tang, Versatile applications of electrochemical flow-through systems in water treatment processes, Chem. Eng. J. 473 (2023), 145400.

[8] X. Li, W. Xing, T. Hu, K. Luo, J. Wang, W. Tang, Recent advances in transition-metal phosphide electrocatalysts: synthetic approach, improvement strategies and environmental applications, Coord. Chem. Rev. 473 (2022), 214811.

[9] Y.-W. Lu, X.-X. Liang, C.-Y. Wang, D. Chen, H. Liu, Synergistic nanowire-assisted electroporation and chlorination for inactivation of chlorine-resistant bacteria in drinking water systems via inducing cell pores for chlorine permeation, Water Res. 229 (2023), 119399.

[10] M. Liu, N. Graham, W. Wang, R. Zhao, Y. Lu, M. Elimelech, W. Yu, Spatial assessment of tap-water safety in China, Nat. Sustain. 5 (2022) 689–698.

[11] L. Ding, L. Li, Y. Liu, Y. Wu, Z. Lu, J. Deng, Y. Wei, J. Caro, H. Wang, Effective ion sieving with $Ti_3C_2T_x$ MXene membranes for production of drinking water from seawater, Nat. Sustain. 3 (2020) 296–302.

[12] I. Jeon, E.C. Ryberg, P.J.J. Alvarez, J.-H. Kim, Technology assessment of solar disinfection for drinking water treatment, Nat. Sustain. 5 (2022) 801–808.

[13] J. Zhang, D. Wang, F. Zhao, J. Feng, H. Feng, J. Luo, W. Tang, Ferrate modified carbon felt as excellent heterogeneous electro-Fenton cathode for chloramphenicol degradation, Water Res. 227 (2022), 119324.

[14] T. Hu, L. Tang, H. Feng, J. Zhang, X. Li, Y. Zuo, Z. Lu, W. Tang, Metal-organic frameworks (MOFs) and their derivatives as emerging catalysts for electro-Fenton process in water purification, Coord. Chem. Rev. 451 (2022), 214277.

[15] Y. Wang, C. Liang, C. Fan, J. Chen, Z. Zhang, H. Liu, Composite modification of carbon fiber cathode with tree-like branched polypyrrole-microwires and polyaniline-nanorods for enhancing hexavalent chromium reduction, Environ. Sci. Nano 10 (2023) 891–901.

[16] Y. Wang, G.I.N. Waterhouse, L. Shang, T. Zhang, Electrocatalytic oxygen reduction to hydrogen peroxide: from homogeneous to heterogeneous electrocatalysis, Adv. Energy Mater. 11 (2021), 2003323.

[17] X. Yang, Y. Zeng, W. Alnoush, Y. Hou, D. Higgins, G. Wu, Tuning two-electron oxygen-reduction pathways for H_2O_2 electrosynthesis via engineering atomically dispersed single metal site catalysts, Adv. Mater. 34 (2022), 2107954.

[18] T. Richards, J.H. Harrhy, R.J. Lewis, A.G.R. Howe, G.M. Suldecki, A. Folli, D. J. Morgan, T.E. Davies, E.J. Loveridge, D.A. Crole, J.K. Edwards, P. Gaskin, C. J. Kiely, Q. He, D.M. Murphy, J.-Y. Maillard, S.J. Freakley, G.J. Hutchings, A residue-free approach to water disinfection using catalytic in situ generation of reactive oxygen species, Nat. Catal. 4 (2021) 575–585.

[19] J. Xu, X. Zheng, Z. Feng, Z. Lu, Z. Zhang, W. Huang, Y. Li, D. Vuckovic, Y. Li, S. Dai, G. Chen, K. Wang, H. Wang, J.K. Chen, W. Mitch, Y. Cui, Organic wastewater treatment by a single-atom catalyst and electrolytically produced H_2O_2, Nat. Sustain. 4 (2021) 233–241.

[20] J. Li, J. You, Z. Wang, Y. Zhao, J. Xu, X. Li, H. Zhang, Application of α-Fe_2O_3-based heterogeneous photo-Fenton catalyst in wastewater treatment: a review of recent advances, J. Environ. Chem. Eng. 10 (2022), 108329.

[21] X.-C. Liu, K.-X. Zhang, J.-S. Song, G.-N. Zhou, W.-Q. Li, R.-R. Ding, J. Wang, X. Zheng, G. Wang, Y. Mu, Tuning Fe_3O_4 for sustainable cathodic heterogeneous electro-Fenton catalysis by acetylated chitosan, Proc. Natl. Acad. Sci. USA 120 (2023), e2213480120.

[22] Y. Chen, C.J. Miller, R.N. Collins, T.D. Waite, Key considerations when assessing novel fenton catalysts: iron oxychloride (FeOCl) as a case study, Environ. Sci. Technol. 55 (2021) 13317–13325.

[23] L. Cui, X. Zhao, H. Xie, Z. Zhang, Overcoming the activity–stability trade-off in heterogeneous electro-fenton catalysis: encapsulating carbon cloth-supported iron oxychloride within graphitic layers, ACS Catal. 12 (2022) 13334–13348.

[24] J. Wang, K.P. Hou, Y. Wen, H. Liu, H. Wang, K. Chakarawet, M. Gong, X. Yang, Interlayer structure manipulation of iron oxychloride by potassium cation intercalation to steer H_2O_2 activation pathway, J. Am. Chem. Soc. 144 (2022) 4294–4299.

[25] J. Wang, S. Li, Q. Qin, C. Peng, Sustainable and feasible reagent-free electro-Fenton via sequential dual-cathode electrocatalysis, Proc. Natl. Acad. Sci. USA 118 (2021), e2108573118.

[26] X. Xu, Y. Zhang, Y. Chen, C. Liu, W. Wang, J. Wang, H. Huang, J. Feng, Z. Li, Z. Zou, Revealing *OOH key intermediates and regulating H_2O_2 photoactivation by surface relaxation of Fenton-like catalysts, Proc. Natl. Acad. Sci. USA 119 (2022), e2205562119.

[27] Y. Liu, S. Yin, P.K. Shen, Asymmetric 3d electronic structure for enhanced oxygen evolution catalysis, ACS Appl. Mater. Interfaces 10 (2018) 23131–23139.

[28] Y. Zhao, T. Ling, S. Chen, B. Jin, A. Vasileff, Y. Jiao, L. Song, J. Luo, S.-Z. Qiao, Non-metal single-iodine-atom electrocatalysts for the hydrogen evolution reaction, Angew. Chem. Int. Ed. 58 (2019) 12252–12257.

[29] Q. Tu, W. Liu, M. Jiang, W. Wang, Q. Kang, P. Wang, W. Zhou, F. Zhou, Preferential adsorption of hydroxide ions onto partially crystalline NiFe-layered double hydroxides leads to efficient and selective OER in alkaline seawater, ACS Appl. Energy Mater. 4 (2021) 4630–4637.

[30] E. Brillas, I. Sirés, M.A. Oturan, Electro-Fenton process and related electrochemical technologies based on Fenton's reaction chemistry, Chem. Rev. 109 (2009) 6570–6631.

[31] E. Brillas, Fenton, photo-Fenton, electro-Fenton, and their combined treatments for the removal of insecticides from waters and soils. A review, Sep. Purif. Technol. 284 (2022), 120290.

[32] S.O. Ganiyu, M. Zhou, C.A. Martínez-Huitle, Heterogeneous electro-Fenton and photoelectro-Fenton processes: a critical review of fundamental principles and application for water/wastewater treatment, Appl. Catal. B-Environ. 235 (2018) 103–129.

[33] X. Wang, Q. Zhang, J. Jing, G. Song, M. Zhou, Biomass derived S, N self-doped catalytic Janus cathode for flow-through metal-free electrochemical advanced oxidation process: better removal efficiency and lower energy consumption under neutral conditions, Chem. Eng. J. 466 (2023), 143283.

[34] P. Wu, Y. Zhang, Z. Chen, Y. Duan, Y. Lai, Q. Fang, F. Wang, S. Li, Performance of boron-doped graphene aerogel modified gas diffusion electrode for in-situ metal-free electrochemical advanced oxidation of Bisphenol A, Appl. Catal. B-Environ. 255 (2019), 117784.

[35] Y. Li, W. Cao, X. Zuo, O- and F-doped porous carbon bifunctional catalyst derived from polyvinylidene fluoride for sulfamerazine removal in the metal-free electro-Fenton process, Environ. Res. 212 (2022), 113508.

[36] D. Guo, R. Shibuya, C. Akiba, S. Saji, T. Kondo, J. Nakamura1, Active sites of nitrogen-doped carbon materials for oxygen reduction reaction clarified using model catalysts, Science 351 (2016) 361–365.

[37] J. Deng, D. Deng, X. Bao, Robust catalysis on 2D materials encapsulating metals: concept, application, and perspective, Adv. Mater. 29 (2017) 1606967.

[38] W. Jin, J. Feng, W. Xing, W. Tang, Significantly enhanced electrocatalytic reduction of chloramphenicol from water mediated by Fe–F–N Co-doped carbon materials, ACS EST Water 3 (2023) 1385–1394.

[39] D. Xu, S.-N. Zhang, J.-S. Chen, X.-H. Li, Design of the synergistic rectifying interfaces in Mott–Schottky catalysts, Chem. Rev. 123 (2023) 1–30.

[40] J. Su, G.D. Li, X.H. Li, J.S. Chen, 2D/2D heterojunctions for catalysis, Adv. Sci. 6 (2019) 1801702.

[41] M.R. Haider, W.L. Jiang, J.L. Han, A. Mahmood, R. Djellabi, H. Liu, M.B. Asif, A. J. Wang, Boosting hydroxyl radical yield via synergistic activation of electrogenerated $HOCl/H_2O_2$ in electro-fenton-like degradation of contaminants under chloride conditions, Environ. Sci. Technol. (2023). ⟨https://pubs.acs.org/doi/10.1021/acs.est.2c07752⟩.

[42] M.R. Haider, W.-L. Jiang, J.-L. Han, H.M.A. Sharif, Y.-C. Ding, H.-Y. Cheng, A.-J. Wang, In-situ electrode fabrication from polyaniline derived N-doped carbon nanofibers for metal-free electro-Fenton degradation of organic contaminants, Appl. Catal. B-Environ. 256 (2019), 117774.

[43] P. Su, M. Zhou, X. Lu, W. Yang, G. Ren, J. Cai, Electrochemical catalytic mechanism of N-doped graphene for enhanced H_2O_2 yield and in-situ degradation of organic pollutant, Appl. Catal. B-Environ. 245 (2019) 583–595.

[44] M. Sun, C. Chu, F. Geng, X. Lu, J. Qu, J. Crittenden, M. Elimelech, J.-H. Kim, Reinventing Fenton chemistry: iron oxychloride nanosheet for pH-insensitive H_2O_2 activation, Environ. Sci. Technol. Lett. 5 (2018) 186–191.

[45] Xianliang Zhou, K. Mopper, Determination of photochemically produced hydroxyl radicals in seawater and freshwater, Mar. Chem. 30 (1990) 71–88.

[46] G. Kresse, J. Furthmüller, Efficiency of ab-initio total energy calculations for metals and semiconductors using a plane-wave basis set, Comp. Mater. Sci. 6 (1996) 15–50.

[47] J.P. Perdew, K. Burke, M. Ernzerhof, Generalized gradient approximation made simple, Phys. Rev. Lett. 77 (1996) 3865.

[48] V. Wang, N. Xu, J.-C. Liu, G. Tang, W.-T. Geng, VASPKIT: a user-friendly interface facilitating high-throughput computing and analysis using VASP code, Comput. Phys. Commun. 267 (2021), 108033.

[49] G. Henkelman, B.P. Uberuaga, H. Jónsson, A climbing image nudged elastic band method for finding saddle points and minimum energy paths, J. Chem. Phys. 113 (2000) 9901–9904.

[50] G. Henkelman, H. Jónsson, A dimer method for finding saddle points on high dimensional potential surfaces using only first derivatives, J. Chem. Phys. 111 (1999) 7010–7022.

[51] H. Jin, J. Wang, D. Su, Z. Wei, Z. Pang, Y. Wang, In situ cobalt–cobalt oxide/N-doped carbon hybrids as superior bifunctional electrocatalysts for hydrogen and oxygen evolution, J. Am. Chem. Soc. 137 (2015) 2688–2694.

[52] S. Gao, Y. Lin, X. Jiao, Y. Sun, Q. Luo, W. Zhang, D. Li, J. Yang, Y. Xie, Partially oxidized atomic cobalt layers for carbon dioxide electroreduction to liquid fuel, Nature 529 (2016) 68–71.

[53] V.G. Hadjiev, M.N. Iliev, I.V. Vergilov, The Raman spectra of Co_3O_4, J. Phys. C 21 (1988) L199.

[54] X. Wen, J. Miao, D. Mandler, M. Long, Rotating ring-disk electrode method to evaluate performance of electrocatalysts in hydrogen peroxide activation via rapid detection of hydroxyl radicals, Chem. Eng. J. 454 (2023), 140312.

[55] C. Weng, Y.-H. Chuang, B. Davey, W.A. Mitch, Reductive electrochemical activation of hydrogen peroxide as an advanced oxidation process for treatment of reverse osmosis permeate during potable reuse, Environ. Sci. Technol. 54 (2020) 12593–12601.

[56] B.-H. Lee, H. Shin, A.S. Rasouli, H. Choubisa, P. Ou, R. Dorakhan, I. Grigioni, G. Lee, E. Shirzadi, R.K. Miao, J. Wicks, S. Park, H.S. Lee, J. Zhang, Y. Chen, Z. Chen, D. Sinton, T. Hyeon, Y.-E. Sung, E.H. Sargent, Supramolecular tuning of supported metal phthalocyanine catalysts for hydrogen peroxide electrosynthesis, Nat. Catal. 6 (2023) 234–243.

[57] K. Gelderman, L. Lee, S.W. Donne, Flat-band potential of a semiconductor: using the Mott–Schottky equation, J. Chem. Educ. 84 (2007) 685–688.